submitted to *Geophys. J. Int.*

Magnetic data radial inversion for 3-D source geometry estimation

L.B. Vital[1*]

[1] *Observatório Nacional, Gal. José Cristino, 77, São Cristóvão, Rio de Janeiro, 20921-400, Brazil*

Key words: Numerical solutions; Inverse theory; Magnetic anomalies.

* Observatório Ncional, ON

1 METHODOLOGY

1.1 Forward problem

Let $\mathbf{d}^o$ be the observed data vector, whose ith element d_i^o, $i = 1, \ldots, N$, is the total-field anomaly produced by a 3-D source (Fig. 1a) at the point (x_i, y_i, z_i) of a Cartesian coordinate system with x, y and z axes pointing to north, east and down, respectively. We assume that the direction of the total magnetization vector of the source is constant and known. We approximate the volume of the source by a set of L vertically juxtaposed 3-D prisms (Fig. 1b) by following the same approach of Oliveira Jr. et al. (2011) and Oliveira Jr. & Barbosa (2013). The depth to the top of the shallowest prism is defined by z_0 and m_0 is the constant total-magnetization intensity of all prisms. The horizontal cross-section of each prism is described by a polygon with a fixed number V of vertices equally spaced from $0°$ to $360°$, which are described in polar coordinates referred to an internal origin O^k . The radii of the vertices (r_j^k, $j = 1, \ldots, V$, $k = 1, \ldots, L$), the horizontal coordinates (x_0^k and y_0^k, $k = 1, \ldots, L$) of the origins O^k, $k = 1, \ldots, L$, and the depth extent dz of the L vertically stacked prisms (Fig. 1b) are arranged in a $M \times 1$ parameter vector $\mathbf{p}$, $M = L(V + 2) + 1$, given by

$$\mathbf{p} = \begin{bmatrix} \mathbf{r}^{1\top} & x_0^1 & y_0^1 & \ldots & \mathbf{r}^{L\top} & x_0^L & y_0^L & dz \end{bmatrix}^\top , \tag{1}$$

where "$^\top$" denotes transposition and $\mathbf{r}^k$ is a $V \times 1$ vector containing the radii r_j^k of the kth prism. Let $\mathbf{d}(\mathbf{p})$ be the predicted data vector, whose ith element

$$d_i(\mathbf{p}) \equiv \sum_{k=1}^{L} f_i^k(\mathbf{r}^k, x_0^k, y_0^k, dz, z_1^k, m_0), \quad i = 1, \ldots, N , \tag{2}$$

is the total-field anomaly produced by the ensemble of L prisms at the ith observation point (x_i, y_i, z_i). In eq. 2, $f_i^k(\mathbf{r}^k, x_0^k, y_0^k, dz, z_1^k, m_0)$ is the total-field anomaly produced, at the observation point (x_i, y_i, z_i), by the kth prism, with depth to the top $z_1^k = z_0 + (k - 1)dz$. We calculate $d_i(\mathbf{p})$ (eq. 2) by using the Python package Fatiando a Terra (Uieda et al. 2013), which implements the formulas proposed by Plouff (1976).

1.2 Inverse problem formulation

Given a set of tentative values for depth to the top of the shallowest prism z_0 and for the intensity of the total-magnetization of the source m_0, we solve a constrained non-linear problem to estimate the parameter vector $\mathbf{p}$ (eq. 1) by minimizing the goal function

$$\Gamma(\mathbf{p}) = \phi(\mathbf{p}) + \sum_{\ell=1}^{7} \alpha_\ell \, \varphi_\ell(\mathbf{p}) , \tag{3}$$

subject to

$$p_l^{min} < p_l < p_l^{max}, \quad l = 1, \dots, M \ , \tag{4}$$

where $\varphi(\mathbf{p})$ is the data-misfit function given by

$$\phi(\mathbf{p}) = \frac{1}{N} \| \mathbf{d}^o - \mathbf{d}(\mathbf{p}) \|_2^2 \ , \tag{5}$$

which represents the normalized squared Euclidean norm of the difference between the observed data vector $\mathbf{d}^o$ and the predicted data vector $\mathbf{d}(\mathbf{p})$, α_ℓ is a positive number representing the weight of the ℓth constraint function $\varphi_\ell(\mathbf{p})$ and p_l^{min} and p_l^{max} are, respectively, the lower and upper limits for the lth element p_l of the parameter vector $\mathbf{p}$ (eq. 1). These limits are defined by the interpreter based on both the horizontal extent of the magnetic anomaly and the knowledge about the source.

To solve our nonlinear inverse problem, we use a gradient-based method and, consequently, we need to define the gradient vector $\boldsymbol{\nabla}\Gamma(\mathbf{p})$ and Hessian matrix $\mathbf{H}(\mathbf{p})$ of the goal function $\Gamma(\mathbf{p})$ (eq. 3):

$$\boldsymbol{\nabla}\Gamma(\mathbf{p}) = \boldsymbol{\nabla}\phi(\mathbf{p}) + \sum_{\ell=1}^{7} \alpha_\ell \, \boldsymbol{\nabla}\varphi_\ell(\mathbf{p}) \tag{6}$$

and

$$\mathbf{H}(\mathbf{p}) = \mathbf{H}_\phi(\mathbf{p}) + \sum_{\ell=1}^{7} \alpha_\ell \, \mathbf{H}_\ell \ , \tag{7}$$

where

$$\boldsymbol{\nabla}\phi(\mathbf{p}) = -\frac{2}{N} \mathbf{G}(\mathbf{p})^{\mathsf{T}} [\mathbf{d}^o - \mathbf{d}(\mathbf{p})] \tag{8}$$

and

$$\mathbf{H}_\phi(\mathbf{p}) = \frac{2}{N} \mathbf{G}(\mathbf{p})^{\mathsf{T}} \mathbf{G}(\mathbf{p}) \tag{9}$$

are the gradient vector of the Hessian matrix of the misfit function $\phi(\mathbf{p})$ (eq. 5), respectively, the terms $\boldsymbol{\nabla}\varphi_\ell(\mathbf{p})$ and $\mathbf{H}_\ell$, $\ell = 1, \dots, 7$, are the gradient vectors and Hessian matrices of the constraint functions, respectively, and $\mathbf{G}(\mathbf{p})$ is an $N \times M$ matrix whose element ij is the derivative of the predicted data $d_i(\mathbf{p})$ (eq. 2) with respect to the j element p_j of the parameter vector $\mathbf{p}$ (eq. 1). Details about the constraint functions $\varphi_\ell(\mathbf{p})$, $\ell = 1, \dots, 7$, as well as the numerical procedure to solve this nonlinear inverse problem are given in the following sections.

1.3 Constraint functions

We have divided the constraint functions $\varphi_\ell(\mathbf{p})$ (eq. 3), $\ell = 1, \dots, 7$, used here to obtain stable solutions and introduce a priori information about the magnetic source into three groups.

1.3.1 Smoothness constraints

This group is formed by variations of the first-order Tikhonov regularization (Aster et al. 2019, p. 103) and impose smoothness on the radii r_j^k and the Cartesian coordinates x_0^k and y_0^k of the origin O^k, $j = 1, \ldots, V$, $k = 1, \ldots, L$, defining the horizontal section of each prism (Fig. 1b). They were proposed by Oliveira Jr. et al. (2011) and Oliveira Jr. & Barbosa (2013) and play a very role in introducing a prior information about the shape of the source.

The first constraint of this group is the *Smoothness constraint on the adjacent radii defining the horizontal section of each vertical prism*. This constraint imposes that adjacent radii r_j^k and r_{j+1}^k within each prism must be close to each other. It forces the estimated prism to be approximately cylindrical. Mathematically, the constraint is given by

$$\begin{aligned}\varphi_1(\mathbf{p}) &= \sum_{k=1}^{L} \left[\left(r_V^k - r_1^k \right)^2 + \sum_{j=1}^{V-1} \left(r_j^k - r_{j+1}^k \right)^2 \right] \\ &= \mathbf{p}^{\mathsf{T}} \mathbf{R}_1^{\mathsf{T}} \mathbf{R}_1 \mathbf{p} \quad , \end{aligned} \tag{10}$$

where

$$\mathbf{S}_1 = \mathbf{I}_L \otimes \left[\left(\mathbf{I}_V - \mathbf{D}_V^{\mathsf{T}} \right) \quad \mathbf{0}_{V \times 2} \right] \quad , \tag{11}$$

$\mathbf{0}_{LV \times 1}$ is an $LV \times 1$ vector with null elements, $\mathbf{I}_L$ is the identity matrix of order L, "$\otimes$" denotes the Kronecker product (Horn & Johnson 1991, p. 243), $\mathbf{0}_{V \times 2}$ is a $V \times 2$ matrix with null elements, $\mathbf{I}_V$ is the identity matrix of order V and $\mathbf{D}_V^{\mathsf{T}}$ is the upshift permutation matrix of order V (Golub & Loan 2013, p. 20). The gradient and Hessian of function $\varphi_1(\mathbf{p})$ (eq. 10) are given by:

$$\boldsymbol{\nabla} \varphi_1(\mathbf{p}) = 2 \mathbf{R}_1^{\mathsf{T}} \mathbf{R}_1 \mathbf{p} \quad , \tag{12}$$

and

$$\mathbf{H}_1(\mathbf{p}) = 2 \mathbf{R}_1^{\mathsf{T}} \mathbf{R}_1 \quad . \tag{13}$$

The second constraint of this group is the *Smoothness constraint on the adjacent radii of the vertically adjacent prisms*, which imposes that adjacent radii r_j^k and r_j^{k+1} within vertically adjacent prisms must be close to each other. This constraint forces the shape of all prisms to be similar to each other and is given by

$$\begin{aligned}\varphi_2(\mathbf{p}) &= \sum_{k=1}^{L-1} \left[\sum_{j=1}^{V} \left(r_j^{k+1} - r_j^k \right)^2 \right] \quad , \\ &= \mathbf{p}^{\mathsf{T}} \mathbf{R}_2^{\mathsf{T}} \mathbf{R}_2 \mathbf{p} \end{aligned} \tag{14}$$

where

$$\mathbf{R}_2 = \begin{bmatrix} \mathbf{S}_2 & \mathbf{0}_{(L-1)V\times 1} \end{bmatrix}_{(L-1)V\times M} \quad , \tag{15}$$

$$\mathbf{S}_2 = \left(\begin{bmatrix} \mathbf{I}_{L-1} & \mathbf{0}_{(L-1)\times 1} \end{bmatrix} - \begin{bmatrix} \mathbf{0}_{(L-1)\times 1} & \mathbf{I}_{L-1} \end{bmatrix} \right) \otimes \begin{bmatrix} \mathbf{I}_V & \mathbf{0}_{V\times 2} \end{bmatrix} \quad , \tag{16}$$

$\mathbf{0}_{(L-1)V\times 1}$ is an $(L-1)V \times 1$ vector with null elements, $\mathbf{0}_{(L-1)\times 1}$ is an $(L-1)\times 1$ vector with null elements and $\mathbf{I}_{L-1}$ is the identity matrix of order $L-1$. The gradient and Hessian of function $\varphi_2(\mathbf{p})$ (eq. 14) are given by:

$$\boldsymbol{\nabla}\varphi_2(\mathbf{p}) = 2\mathbf{R}_2^{\mathsf{T}}\mathbf{R}_2\mathbf{p} \quad , \tag{17}$$

and

$$\mathbf{H}_2(\mathbf{p}) = 2\mathbf{R}_2^{\mathsf{T}}\mathbf{R}_2 \quad . \tag{18}$$

The last constraint of this group is the *Smoothness constraint on the horizontal position of the arbitrary origins of the vertically adjacent prisms*. This constraint imposes that the estimated horizontal Cartesian coordinates (x_0^k, y_0^k) and (x_0^{k+1}, y_0^{k+1}) of the origins O^k and O^{k+1} of adjacent prisms must be close to each other. It forces the prisms to be vertically aligned. This constraint is given by

$$\begin{aligned} \varphi_3(\mathbf{p}) &= \sum_{k=1}^{L-1} \left[\left(x_0^{k+1} - x_0^k \right)^2 + \left(y_0^{k+1} - y_0^k \right)^2 \right] \quad , \\ &= \mathbf{p}^{\mathsf{T}}\mathbf{R}_3^{\mathsf{T}}\mathbf{R}_3\mathbf{p} \end{aligned} \tag{19}$$

where

$$\mathbf{R}_3 = \begin{bmatrix} \mathbf{S}_3 & \mathbf{0}_{(L-1)2\times 1} \end{bmatrix}_{(L-1)2\times M} \quad , \tag{20}$$

$$\mathbf{S}_3 = \left(\begin{bmatrix} \mathbf{I}_{L-1} & \mathbf{0}_{(L-1)\times 1} \end{bmatrix} - \begin{bmatrix} \mathbf{0}_{(L-1)\times 1} & \mathbf{I}_{L-1} \end{bmatrix} \right) \otimes \begin{bmatrix} \mathbf{0}_{2\times V} & \mathbf{I}_2 \end{bmatrix} \quad , \tag{21}$$

$\mathbf{0}_{(L-1)2\times 1}$ is an $(L-1)2\times 1$ vector with null elements, $\mathbf{0}_{2\times V}$ is a $2\times V$ matrix with null elements and $\mathbf{I}_2$ is the identity matrix of order 2. The gradient and Hessian of function $\varphi_3(\mathbf{p})$ (eq. 19) are given by:

$$\boldsymbol{\nabla}\varphi_3(\mathbf{p}) = 2\mathbf{R}_3^{\mathsf{T}}\mathbf{R}_3\mathbf{p} \quad , \tag{22}$$

and

$$\mathbf{H}_3(\mathbf{p}) = 2\mathbf{R}_3^{\mathsf{T}}\mathbf{R}_3 \quad . \tag{23}$$

1.3.2 Equality constraints

This group if formed by two constraints that were proposed by Oliveira Jr. et al. (2011) and Oliveira Jr. & Barbosa (2013) by following the same approach proposed Barbosa et al. (1997) and **?**). They introduce a priori information about the shallowest prism and are suitable for outcropping sources.

The *Source's outcrop constraint* imposes that the horizontal cross-section of the shallowest prism must be close to the intersection of the geologic source with the known outcropping boundary. The matrix form of the this constraint is given by

$$\begin{aligned}\varphi_4(\mathbf{p}) &= \left[\left(x_0^1 - x_0^0\right)^2 + \left(y_0^1 - y_0^0\right)^2 + \sum_{j=1}^{V}\left(r_j^1 - r_j^0\right)^2\right] \\ &= \left(\mathbf{R}_4\mathbf{p} - \mathbf{a}\right)^{\mathsf{T}}\left(\mathbf{R}_4\mathbf{p} - \mathbf{a}\right)\end{aligned}, \tag{24}$$

where $\mathbf{a}$ is a vector containing the radii and the horizontal Cartesian coordinates of the polygon defining the outcropping boundary

$$\mathbf{a} = \begin{bmatrix}\tilde{r}_1^0 & \dots & \tilde{r}_V^0 & \tilde{x}_0^0 & \tilde{y}_0^0\end{bmatrix}^{\mathsf{T}}, \tag{25}$$

and

$$\mathbf{R}_4 = \begin{bmatrix}\mathbf{I}_{V+2} & \mathbf{0}_{(V+2)\times(M-V-2)}\end{bmatrix}_{(V+2)\times M}, \tag{26}$$

where $\mathbf{I}_{V+2}$ is the identity matrix of order $V+2$ and $\mathbf{0}_{(V+2)\times(M-V-2)}$ is a matrix with null elements. The gradient and Hessian of function $\varphi_4(\mathbf{p})$ (eq. 24) are given by:

$$\boldsymbol{\nabla}\varphi_4(\mathbf{p}) = 2\mathbf{R}_4^{\mathsf{T}}\left(\mathbf{R}_4\mathbf{p} - \mathbf{a}\right) \quad , \tag{27}$$

and

$$\mathbf{H}_4(\mathbf{p}) = 2\mathbf{R}_4^{\mathsf{T}}\mathbf{R}_4 \quad . \tag{28}$$

The *Source's horizontal location constraint* imposes that the horizontal Cartesian coordinates of the origin within the shallowest prism must be as close as possible to a known outcropping point. The matrix form of the this constraint is given by

$$\begin{aligned}\varphi_5(\mathbf{p}) &= \left[\left(x_0^1 - x_0^0\right)^2 + \left(y_0^1 - y_0^0\right)^2\right] \\ &= \left(\mathbf{R}_5\mathbf{p} - \mathbf{b}\right)^{\mathsf{T}}\left(\mathbf{R}_5\mathbf{p} - \mathbf{b}\right)\end{aligned}, \tag{29}$$

where $\mathbf{b}$ is a vector containing the horizontal Cartesian coordinates of the outcropping point

$$\mathbf{b} = \begin{bmatrix}\tilde{x}_0^0 & \tilde{y}_0^0\end{bmatrix}^{\mathsf{T}}, \tag{30}$$

and

$$\mathbf{R}_5 = \begin{bmatrix}\mathbf{0}_{2\times V} & \mathbf{I}_2 & \mathbf{0}_{2\times(M-V-2)}\end{bmatrix}_{2\times M}, \tag{31}$$

where $\mathbf{I}_2$ is the identity matrix of order 2 and $\mathbf{0}_{2\times(M-V-2)}$ and $\mathbf{0}_{2\times V}$ are matrices with null elements. The gradient and Hessian of function $\varphi_5(\mathbf{p})$ (eq. 29) are given by:

$$\boldsymbol{\nabla}\varphi_5(\mathbf{p}) = 2\mathbf{R}_5^{\mathsf{T}}\left(\mathbf{R}_5\mathbf{p} - \mathbf{b}\right) \quad , \tag{32}$$

and

$$\mathbf{H}_5(\mathbf{p}) = 2\mathbf{R}_5^{\mathsf{T}}\mathbf{R}_5 \quad . \tag{33}$$

1.3.3 Minimum Euclidean norm constraints

Two constraints use the zeroth-order Tikhonov regularization with the purpose of obtaining stable solutions without necessarily introducing significant a priori information about the source.

The *Minimum Euclidean norm of the radii* imposes that all estimated radii within each prism must be close to null values. This constraint were proposed by Oliveira Jr. et al. (2011) and Oliveira Jr. & Barbosa (2013) and can be rewritten in matrix form as follows

$$\begin{aligned} \varphi_6(\mathbf{p}) &= \sum_{k=1}^{L}\sum_{j=1}^{V}\left(r_j^k\right)^2 \\ &= \mathbf{p}^{\mathsf{T}}\mathbf{R}_6^{\mathsf{T}}\mathbf{R}_6\mathbf{p} \end{aligned} \quad , \tag{34}$$

where

$$\mathbf{R}_6 = \begin{bmatrix} \mathbf{S}_6 & \mathbf{0}_{(M-1)\times 1} \\ \mathbf{0}_{1\times(M-1)} & 0 \end{bmatrix}_{M\times M} \quad , \tag{35}$$

and

$$\mathbf{S}_6 = \begin{bmatrix} \mathbf{I}_V & \mathbf{0}_{V\times 2} \\ \mathbf{0}_{2\times V} & \mathbf{I}_2 \end{bmatrix}_{(V+2)\times(V+2)} \quad . \tag{36}$$

The gradient and Hessian of function $\varphi_6(\mathbf{p})$ (eq. 34) are given by:

$$\boldsymbol{\nabla}\varphi_6(\mathbf{p}) = 2\mathbf{R}_6^{\mathsf{T}}\mathbf{R}_6\mathbf{p} \quad , \tag{37}$$

and

$$\mathbf{H}_6(\mathbf{p}) = 2\mathbf{R}_6^{\mathsf{T}}\mathbf{R}_6 \quad . \tag{38}$$

The other constraint, the *Minimum Euclidean norm of the depth extent*, imposes that the depth extent of all prisms must be close to zero. We present this constraint to introduce a priori information about the maximum depth of the source. It is given by

$$\begin{aligned} \varphi_7(\mathbf{p}) &= dz^2 \\ &= \mathbf{p}^{\mathsf{T}}\mathbf{R}_7^{\mathsf{T}}\mathbf{R}_7\mathbf{p} \end{aligned} \quad , \tag{39}$$

where

$$\mathbf{R}_7 = \begin{bmatrix} \mathbf{0}_{(M-1)\times(M-1)} & \mathbf{0}_{(M-1)\times 1} \\ \mathbf{0}_{1\times(M-1)} & 1 \end{bmatrix}_{M\times M} \quad . \tag{40}$$

The gradient and Hessian of function $\varphi_7(\mathbf{p})$ (eq. 39) are given by:

$$\boldsymbol{\nabla}\varphi_7(\mathbf{p}) = 2\mathbf{R}_7^{\mathsf{T}}\mathbf{R}_7\mathbf{p} \quad , \tag{41}$$

and

$$\mathbf{H}_7(\mathbf{p}) = 2\mathbf{R}_7^{\mathsf{T}}\mathbf{R}_7 \quad . \tag{42}$$

1.4 Computational procedures

To estimate the parameter vector $\mathbf{p}$ (eq. 1) that minimizes the goal function $\Gamma(\mathbf{p})$ (eq. 3), subjected to the inequality constraint (eq. 4), we use the Levenberg-Marquardt method (e.g., Aster et al. 2019, p. 240). This is an iterative gradient-based method that, at each iteration k, updates the estimated parameter vector $\hat{\mathbf{p}}_{(k)}$ (where the superscript hat "ˆ" denotes estimated) to obtain new a estimated parameter vector $\hat{\mathbf{p}}_{(k+1)}$. We compute this update by following the same strategy of Barbosa et al. (1999b), Oliveira Jr. et al. (2011) and Oliveira Jr. & Barbosa (2013) to incorporate the inequality constraint (eq. 4). This strategy consists in transforming each element p_l of the estimated parameter vector $\hat{\mathbf{p}}_{(k)}$ into the element $p_l^{\dagger}$ of a new vector $\hat{\mathbf{p}}_{(k)}^{\dagger}$ as follows:

$$p_l^{\dagger} = -\ln\left(\frac{p_l^{max} - p_l}{p_l - p_l^{min}}\right) \; , \tag{43}$$

where p_l^{min} and p_l^{max} are defined in the inequality constraint (eq. 4). Then, we compute a correction $\boldsymbol{\Delta}\hat{\mathbf{p}}_{(k)}^{\dagger}$ and a new vector $\hat{\mathbf{p}}_{(k+1)}^{\dagger} = \hat{\mathbf{p}}_{(k)}^{\dagger} + \boldsymbol{\Delta}\hat{\mathbf{p}}_{(k)}^{\dagger}$. Finally, we transform each element $p_l^{\dagger}$ of $\hat{\mathbf{p}}_{(k+1)}^{\dagger}$ into the element p_l of the new estimated parameter vector $\hat{\mathbf{p}}_{(k+1)}$ as follows:

$$p_l = p_l^{min} + \left(\frac{p_l^{max} - p_l^{min}}{1 + e^{-p_l^{\dagger}}}\right) \; . \tag{44}$$

What follows presents details about how we compute the correction $\boldsymbol{\Delta}\hat{\mathbf{p}}_{(k)}^{\dagger}$ and a fully description of our algorithm.

1.4.1 Considerations about the weights $\alpha_1 - \alpha_7$

Attributing values to the weights α_ℓ (eq. 3) is an important feature of our method. However, there is no analytical rule to define them and their values can be dependent on the particular characteristics of the interpretation model. To overcome this problem, we normalize the α_ℓ values as follows:

$$\alpha_\ell = \tilde{\alpha}_\ell \frac{E_\phi}{E_\ell}, \quad \ell = 1, \ldots, 7, \tag{45}$$

where $\tilde{\alpha}_\ell$ is a positive scalar and E_ϕ / E_ℓ is a normalizing factor. In this equation, E_ℓ represents the trace of the Hessian matrix $\mathbf{H}_\ell$ (eqs 13, 18, 23, 28, 33, 38, and 42) of the ℓth constraining function $\varphi_\ell(\mathbf{p})$ (eqs 10, 14, 19, 24, 29, 34, and 39). The constant E_ϕ is the trace of the Hessian matrix $\mathbf{H}_\phi(\mathbf{p}_0)$ (eq.

9) of the misfit function $\phi(\mathbf{p})$ (eq. 5) computed with the initial approximation $\hat{\mathbf{p}}_{(0)}$ for the parameter vector $\mathbf{p}$ (eq. 1) at the beginning of the inversion algorithm. According to this empirical strategy, the weights α_ℓ are defined using the positive scalars $\tilde{\alpha}_\ell$ (eq. 45), which are less dependent on the particular characteristics of the interpretation model.

1.4.2 Inversion algorithm

At each iteration k of our algorithm, the correction $\mathbf{\Delta}\hat{\mathbf{p}}^{\dagger}_{(k)}$ is computed by solving the following linear system:

$$\mathbf{D}_{(k)} \left[\mathbf{D}_{(k)}\mathbf{H}^{\dagger}(\hat{\mathbf{p}}_{(k)})\mathbf{D}_{(k)} + \lambda_{(k)}\mathbf{I}\right] \mathbf{D}_{(k)}\mathbf{\Delta}\hat{\mathbf{p}}^{\dagger}_{(k)} = -\mathbf{\nabla}\Gamma(\hat{\mathbf{p}}_{(k)}) \, , \tag{46}$$

where $\lambda_{(k)}$ is the a positive scalar adjusted at each iteration (e.g., Aster et al. 2019, p. 240), $\mathbf{I}$ is the identity matrix with order M, $\mathbf{\nabla}\Gamma(\hat{\mathbf{p}})$ is the gradient of the goal function (eq. 6) and $\mathbf{H}^{\dagger}(\hat{\mathbf{p}}_{(k)})$ is a matrix given by

$$\mathbf{H}^{\dagger}(\hat{\mathbf{p}}_{(k)}) = \mathbf{H}(\hat{\mathbf{p}}_{(k)})\mathbf{T}(\hat{\mathbf{p}}_{(k)}), \tag{47}$$

where $\mathbf{H}(\hat{\mathbf{p}}_{(k)})$ is the Hessian matrix of the goal function (eq. 7) and $\mathbf{T}(\hat{\mathbf{p}}_{(k)})$ is a diagonal matrix whose element ll is given by

$$t(p_l) = \frac{(p_l^{max} - p_l)(p_l - p_l^{min})}{p_l^{max} - p_l^{min}}, \quad l = 1, \ldots, M \, , \tag{48}$$

with p_l being the lth element of the estimated parameter vector $\hat{\mathbf{p}}_{(k)}$. In eq. 46, $\mathbf{D}_{(k)}$ is a diagonal matrix proposed by Marquardt (1963) for scaling the parameter $\lambda_{(k)}$ at each iteration and improving the convergence of the algorithm. The element ll of this diagonal matrix is given by

$$d_{ll} = \frac{1}{\sqrt{h^{\dagger}_{ll}}} \, , \tag{49}$$

where $h^{\dagger}_{ll}$ is the element ll of the matrix $\mathbf{H}^{\dagger}(\hat{\mathbf{p}}_{(k)})$ (eq. 47). Figure 3 shows a flowchart of our algorithm.

PAREI AQUI

1.4.3 Practical considerations

Our algorithm depends on several parameters that significantly impact the estimated models and cannot be automatically set without the interpreter's judgment. They are the parameters $\tilde{\alpha}_1$, $\tilde{\alpha}_2$, $\tilde{\alpha}_3$, $\tilde{\alpha}_4$, $\tilde{\alpha}_5$, $\tilde{\alpha}_6$, and $\tilde{\alpha}_7$. Based on our practical experience, we suggest some empirical procedures for setting these parameters.

The parameters $\tilde{\alpha}_1$ and $\tilde{\alpha}_2$ impose priori information on the shape of the horizontal cross-section of the prisms. Generally, they have values close to each other varying from 10^{-5} to 10^{-4}. If $\tilde{\alpha}_1 > \tilde{\alpha}_2$ the prisms will have a very smooth horizontal cross-section, close to a circular shape. On the other hand, if $\tilde{\alpha}_1 < \tilde{\alpha}_2$, than the difference on the shape of the horizontal cross-sections of the estimated model between vertically adjacent prisms will be smooth.

To control the alignment of the estimated model, the parameter $\tilde{\alpha}_3$ should be in a range from 10^{-5} to 10^{-3}. This parameter allows or forbids the estimated model to dip. Empirically, the value for this parameter follows the value for $\tilde{\alpha}_1$ and $\tilde{\alpha}_2$, they are usually close.

The parameter $\tilde{\alpha}_6$ imposes mathematical priori information on the inverse problem to control the convergence of the algorithm. We suggest that the value for this parameter should be two or three orders of magnitude greater than $\tilde{\alpha}_1$ and $\tilde{\alpha}_2$.

To control the depth extent of the estimated model, the parameter $\tilde{\alpha}_7$ should be in a range from 10^{-6} to 10^{-4}. This parameter depends on the depth extent of the initial approximate, it can decrease the depth extent or keep it close to the initial one. Normally, we suggest $\tilde{\alpha}_7 = 10^{-5}$ for a initial value.

An important aspect of our method is the choice of the initial approximation. For simplicity, we use a cylinder shape as an initial approximation located the initial cylinder on the center of the anomaly. We suggest that the cylinder radius should involves a great part, both positive and negative, of the horizontal size of the anomaly. Also, the depth extent dz of the cylinder should be greater than the true source. We suggest that the data produced by the initial approximation fit qualitatively the observations.

2 APPLICATION TO SYNTHETIC DATA

2.1 Simple model test

We have simulated a funnel-shaped source with simple geometry (blue prisms in Figs 4b and 6), which extends from $z_0 = 0$ m to 1600 m along depth and satisfies most of the constraints described in subsection 1.3. It is formed by $L = 8$ prisms, all of them with the same number of vertices $V = 20$, depth extent $dz = 200$ m and horizontal coordinates $(x_0^k, y_0^k) = (0, 0)$ m of the origins O^k, $k = 1, \ldots, L$. The radii of all vertices are equal to each other within the same prism and decrease linearly with depth, varying from $r_j^0 = 1920$ m, at the shallowest prism, $r_j^L = 800$ m, at the deepest prism, $j = 1, \ldots, V$. All prisms have the same total-magnetization direction with inclination $-21.5°$, declination $-18.7°$ and intensity $m_0 = 9$ A/m. We calculated the total-field anomaly produced by this simple model on an 100 km^2 area, simulating an airborne survey composed of 21 flight lines that are equally spaced 500 m apart along the y axis, at a constant vertical coordinate $z = -150$ m. At each line, there are 100 observation points spaced 101 m apart along x axis. The total-field anomaly is corrupted with a pseudorandom Gaussian noise having mean $\mu_0 = 0$ nT and and standard deviation $\sigma_0 = 5$ nT (Fig. 4a).

We have inverted the synthetic total-field anomaly (Fig. 4a) produced by the simple model and obtained 36 different models. Each model was obtained by using a different pair of depth to the top z_0 and total-magnetization intensity m_0 (Fig. 5). All models were generated by using the true values of total-magnetization inclination and declination, the same interpretation model formed by $L = 5$ prisms, each one with $V = 20$ vertices, and the same weights for the constraining functions: $\tilde{\alpha}_1 = 10^{-4}$, $\tilde{\alpha}_2 = 10^{-4}$, $\tilde{\alpha}_3 = 10^{-4}$, $\tilde{\alpha}_4 = 0$, $\tilde{\alpha}_5 = 0$, $\tilde{\alpha}_6 = 10^{-6}$, and $\tilde{\alpha}_7 = 10^{-4}$. The initial approximation for all models have the same constant radii $r_j^k = 2000$ m, $k = 1, \ldots, L$, $j = 1, \ldots, V$, the same depth extent $dz = 350$ m and the same origin $(x_0^k, y_0^k) = (0, 0)$ m for all prisms.

Fig. 5 shows that the estimated model obtained by using the true values for depth to the top z_0 and total-magnetization intensity m_0 (represented by the red triangle in Fig. 5) produces the lowest value of goal function $\Gamma(p)$ (eq. 3). Fig. 6a shows that this estimated model (red prisms in Figs 6c and d) not only fits the noise-corrupted data, but also retrieves the geometry of the true model (blue prisms). The inset in Fig. 6a shows that the residuals follow a normal distribution with mean μ and standard deviation σ compatible to μ_0 and σ_0. The estimated depth extent of each prism is $dz = 297.65$ m, which results in a total depth extent (1485 m) very close to the true one (1600 m). These results illustrate the good performance of our method in an ideal case.

2.2 Complex model test

We have simulated a complex inclined body (blue prisms in Figs 7 and 9), which extends from $z_0 = -300$ m to 5700 m along depth and violates most of the constraints described in subsection 1.3. It is formed by $L = 10$ prisms, all of them with the same number of vertices $V = 30$ and depth extent $dz = 600$ m. The horizontal coordinates of the origins O^k vary linearly from $(x_0^0, y_0^0) = (-250, 750)$ m, at the shallowest prism, to $(x_L^0, y_L^0) = (250, -750)$ m resulting a deep in the direction NW-SE, at the deepest prism. The radii $r_j^k, k = 1, \dots, L$, $j = 1, \dots, V$, defining the vertices vary from 240 m to 1540 m and also differ from each other within the same prism. All prisms have a constant total magnetization with inclination $-50°$, declination $9°$ and intensity $m_0 = 12$ A/m. We have calculated the total-field anomaly produced by this complex model on an 100 km^2 area, simulating an airborne survey composed of 18 north-south flight lines distributed from -5000 m to 5000 m along the y axis and a east-west tie line approximately located at $x = 0$ m. The data points are located on the undulated surface shown in Fig. 7a. Notice that both flight and tie lines are not perfectly straight. We added a pseudorandom Gaussian noise having mean μ_0 nT and and standard deviation σ_0 nT to the produced total-field anomaly(Fig. 4a).

Actually, they simulate the real survey presented in the following section. To compute the synthetic total-field anomaly, we consider a constant main field with inclination $-21.5°$ and declination $-18.7°$, which is significantly different from the total-magnetization direction of the complex model. Finally, we have contaminated the synthetic total-field anomaly with a pseudo-random Gaussian noise having mean and standard deviation equal to 0 nT and 5 nT, respectively (Fig. 7a). We have inverted the synthetic total-field anomaly (Fig. 7a) produced by the complex model and to obtain 36 different models. Each model was obtained by using a specific pair of depth to the top z_0 and total-magnetization intensity m_0 (Fig. 8). Differently from the previous simulation with a simple model, the present grid of z_0 and m_0 does not contain the true values (represented by the red triangle in Fig. 8). All models were generated by using the true values of total-magnetization inclination and declination, the same interpretation model formed by $L = 8$ prisms, each one with $V = 15$ vertices, and the same weights for the constraining functions: $\tilde{\alpha}_1 = 10^{-5}$, $\tilde{\alpha}_2 = 10^{-4}$, $\tilde{\alpha}_5 = 10^{-4}$, $\tilde{\alpha}_6 = 10^{-7}$, and $\tilde{\alpha}_7 = 10^{-5}$. The initial approximation for all models have the same constant radii $r_j^k = 800$ m, $k = 1, \dots, L$, $j = 1, \dots, V$, the same depth extent $dz = 650$ m and the same origin $(x_0^k, y_0^k) = (-300, 300)$ m for all prisms.

Fig. 8 shows that the estimated model obtained by using an total- magnetization intensity $m_0 = 11.4$ A/m and a depth to the top $z_0 = -320$ m (represented by the cyan diamond in Fig. 8), close to the true values (represented by the red triangle in Fig. 8), produces the lowest value of goal function $\Gamma(\mathbf{p})$ (eq. 3). Fig. 9 shows that this estimated model (red prisms in Figs 9c and d) fits the noise-corrupted data and also retrieves the geometry of the true source (blue prisms), note that the red prisms edges accurately matches the blue prisms ones. The inset in Fig. 6a shows that the residuals follow a normal distribution with mean μ and standard deviation σ compatible to μ_0 and σ_0. The estimated total depth extent (6145.12 m) and volume (12.81 m^3) are very close to the true values (6000 m and 12.60 m^3). These results show that our method can also be very useful to interpret complex sources, even if they do not perfectly satisfy the constraints imposed to solve the nonlinear inverse problem.

3 APPLICATION TO FIELD DATA

We applied our method to interpret the total-field anomaly data provided by CPRM and acquired by Lasa Prospecções S.A. over the Anitápolis complex in the state of Santa Catarina, Brazil (colocar mapa). The total-field anomaly data were corrected from daytime variation and subtracted from the main field of the Earth using the IGRF. According to Hartmann (citar), Anitápolis is an intrusive complex formed by alkaline-carbonatitic rocks identified using gammaspectrometry and aeromagnetometry of the Brazilian shield. The flight was at an elevation of 100 m above the terrain, the N–S and E–W lines were spaced 500 m and 10,000 m, respectively. We processed the data by applying a regional separation using a second-order polynomial fit. To attenuate the non-dipolar effects present in the data, we applied the equivalent layer to continue the anomaly upward to a constant height $z = -2000$ m (Fig. 10a). The upward continued data were calculated in a regular grid of 50×50 points equally spaced from 6916 km to 6926 km in x axis and 683 km to 693. in y axis. The main field direction in the area at that time has an inclination and declination $(-37.05°, -18.17°)$.

To define the total-magnetization direction of the interpretation model, we used the reduction to the pole (RTP) technique with the main field direction in the area. The RTP result (not shown) indicates that the magnetic source has purely induced magnetization. The interpretation model is formed by an ensemble of $L = 8$ prisms, each one with number of polygon vertices $V = 30$ ($k = 1, \ldots, 10$) describing the horizontal cross-sections of the polygons. We set the origin of the initial approximation $(x_0^k, y_0^k) = (6921, 688)$ km and the radii $r_j^k = 1500$ m so that it involves the center and great part of the positive and negative pols of the anomaly. The depth extent of the prisms is $dz = 700$ m that returns an total-field anomaly in the same range of the observed data. Following the approach for the synthetic applications (sec. 2), we have inverted the real total-field anomaly (Fig. 10a) obtaining 36 different models. Each model was obtained by using a different pair of depth to the top z_0 and total-magnetization intensity m_0 (Fig. 11). For all the 36 models, the initial approximate has the same cylindrical shape and the regularization weights $\tilde{\alpha}_1 = 10^{-3}$, $\tilde{\alpha}_2 = 10^{-4}$, $\tilde{\alpha}_3 = 10^{-3}$, $\tilde{\alpha}_4 = 0$, $\tilde{\alpha}_5 = 0$, $\tilde{\alpha}_6 = 10^{-6}$, and $\tilde{\alpha}_7 = 10^{-5}$. Figs 5 and 8 show that lowest values for $\Gamma(\mathbf{p})$ (eq. 3) indicate the pair of m_0 and z_0 is close to the true one. Therefore, we can interpret that the estimated model that has the pair $z_0 = -900$ m and $m_0 = 5$ A/m (red triangle in Fig. 11) is more realistic than the others. This estimated model produces the best data fit (Fig. 12a) among the 36 inversions. The acceptable fit is confirmed by the histogram of residuals in the inset of the 12a with μ close to zero and a low standard deviation similar to the synthetic applications. Fig. 12b shows the cylinder used as the initial approximate for the inversion. Figs 12c and d show the estimated model (red prisms) for this application. Our method estimated a body northwest-southeast elongated.

ACKNOWLEDGMENTS

REFERENCES

Aster, R. C., Borchers, B., & Thurber, C. H., 2019. *Parameter Estimation and Inverse Problems*, Elsevier, 3rd edn.

Barbosa, V. C. F., Silva, J. B. C., & Medeiros, W. E., 1997. Gravity inversion of basement relief using approximate equality constraints on depths, *Geophysics*, **62**, 1745–1757.

Barbosa, V. C. F., Silva, J. B. C., & Medeiros, W. E., 1999b. Stable inversion of gravity anomalies of sedimentary basins with nonsmooth basement reliefs and arbitrary density contrast variations, *GEOPHYSICS*, **64**(3), 754–764.

Golub, G. H. & Loan, C. F. V., 2013. *Matrix Computations (Johns Hopkins Studies in the Mathematical Sciences)*, Johns Hopkins University Press, 4th edn.

Horn, R. A. & Johnson, C. R., 1991. *Topics in Matrix Analysis*, Cambridge University Press, 1st edn.

Marquardt, D. W., 1963. An algorithm for least-squares estimation of nonlinear parameters, *Journal of the society for Industrial and Applied Mathematics*, **11**(2), 431–441.

Oliveira Jr., V. C. & Barbosa, V. C. F., 2013. 3-D radial gravity gradient inversion, *Geophysical Journal International*, **195**(2), 883–902.

Oliveira Jr., V. C., Barbosa, V. C. F., & Silva, J. B. C., 2011. Source geometry estimation using the mass excess criterion to constrain 3-D radial inversion of gravity data, *Geophysical Journal International*, **187**(2), 754–772.

Plouff, D., 1976. Gravity and magnetic fields of polygonal prisms and application to magnetic terrain corrections, *Geophysics*, **41**(4), 727–741.

Uieda, L., Oliveira Jr., V. C., & Barbosa, V. C. F., 2013. Modeling the earth with fatiando a terra, in *Proceedings of the 12th Python in Science Conference*, pp. 96 – 103.

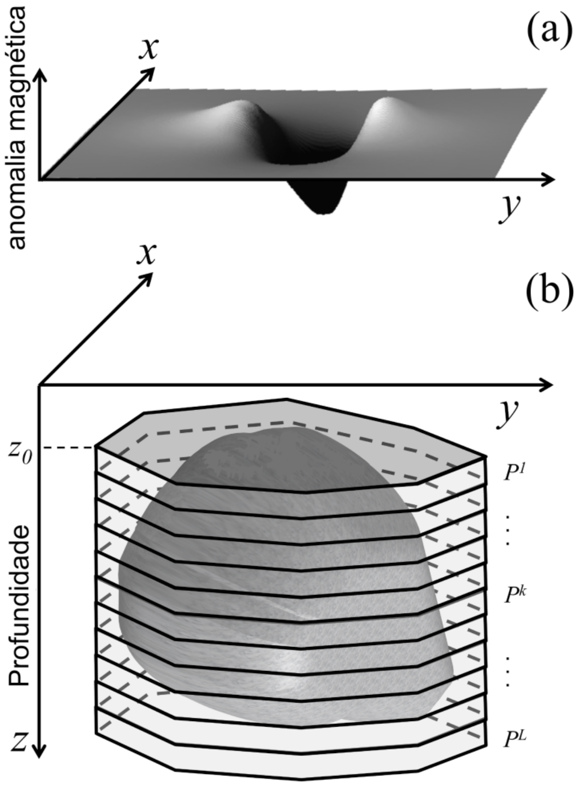

Figure 1. Schematic representation of (a) total-filed anomaly (gray surface) produced by (b) a 3-D anomalous source (dark gray volume). The interpretation model in (b) consists of a set of L vertical, juxtaposed 3-D prisms P^k , $k = 1, \ldots, L$, (light gray prisms) in the vertical direction of a right-handed coordinate system.

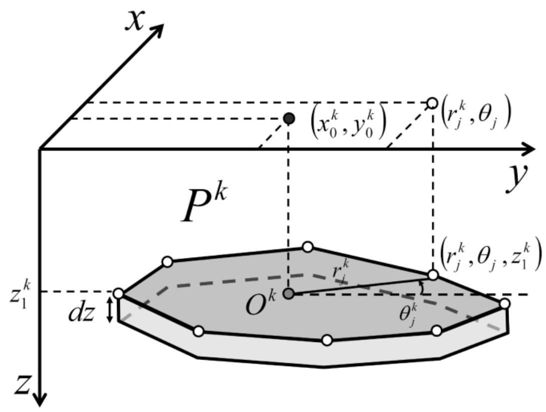

Figure 2. Polygonal cross-section of the kth vertical prism P^k described by V vertices (white dots) with polar coordinates (r_j^k , θ_j^k), $j = 1, \ldots, V$, $k = 1, \ldots, L$, referred to an arbitrary origin O^k (grey dot) with horizontal Cartesian coordinates (x_0^k , y_0^k), $k = 1, \ldots, L$, (black dot).

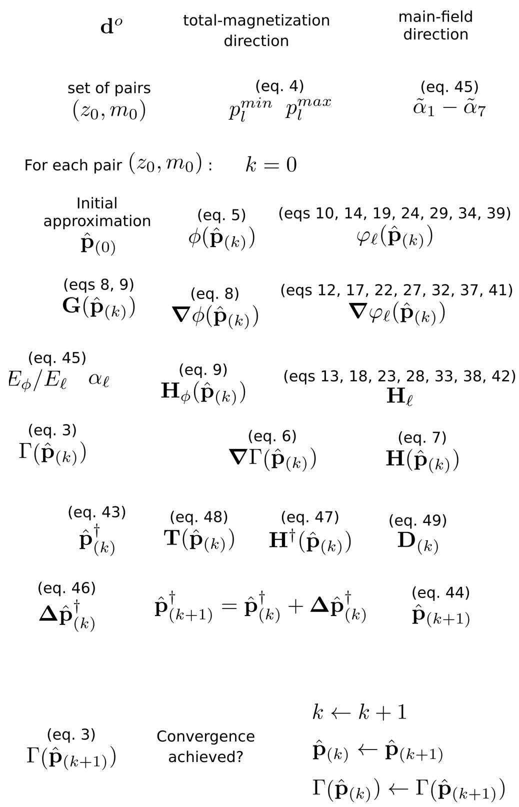

Figure 3. Flowchart of our algorithm.

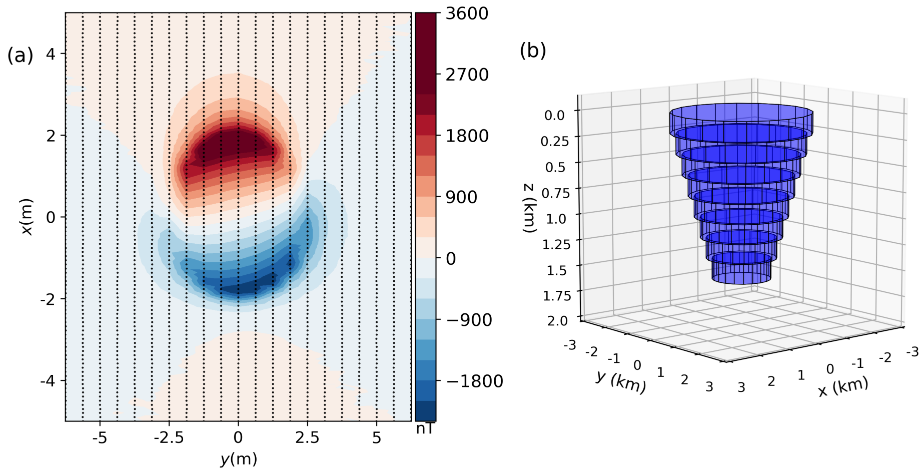

Figure 4. Simple model simulation. (a) noise-corrupted total-field anomaly produced by the simple model (blue prisms) in (b) with a pseudoramdom Gaussian distribution having mean $\mu_0 = 0$ nT and standar deviation $\sigma_0 = 5$ nT, the black dots represent the observation points. (b) perspective view of the simple model represented by the blue prisms.

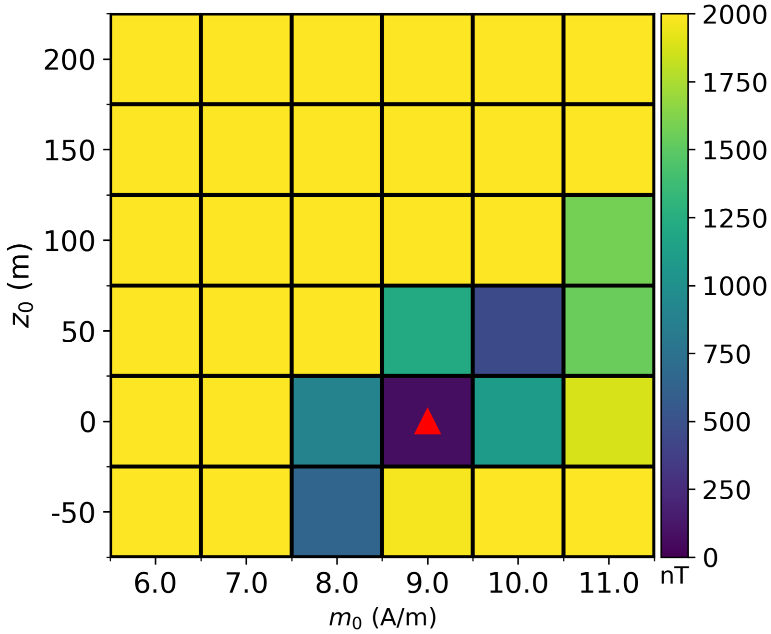

Figure 5. Validation to estimate the depth to the top (z_0) and the total-magnetization intensity (m_0) for the simple model application. The ranges in the axes are $m_0 = 6$ A/m to $m_0 = 11$ A/m with 1 A/m intervals and $z_0 = -50$ m to 200 m with 50 m intervals. Each square is the $\Gamma(\mathbf{p})$ (eq. 3) in nT produced by an estimated model inverted using a pair of m_0 and z_0. These 36 inversions were computed using the same cylinder as a initial approximation. The red triangle represents the true m_0 and z_0.

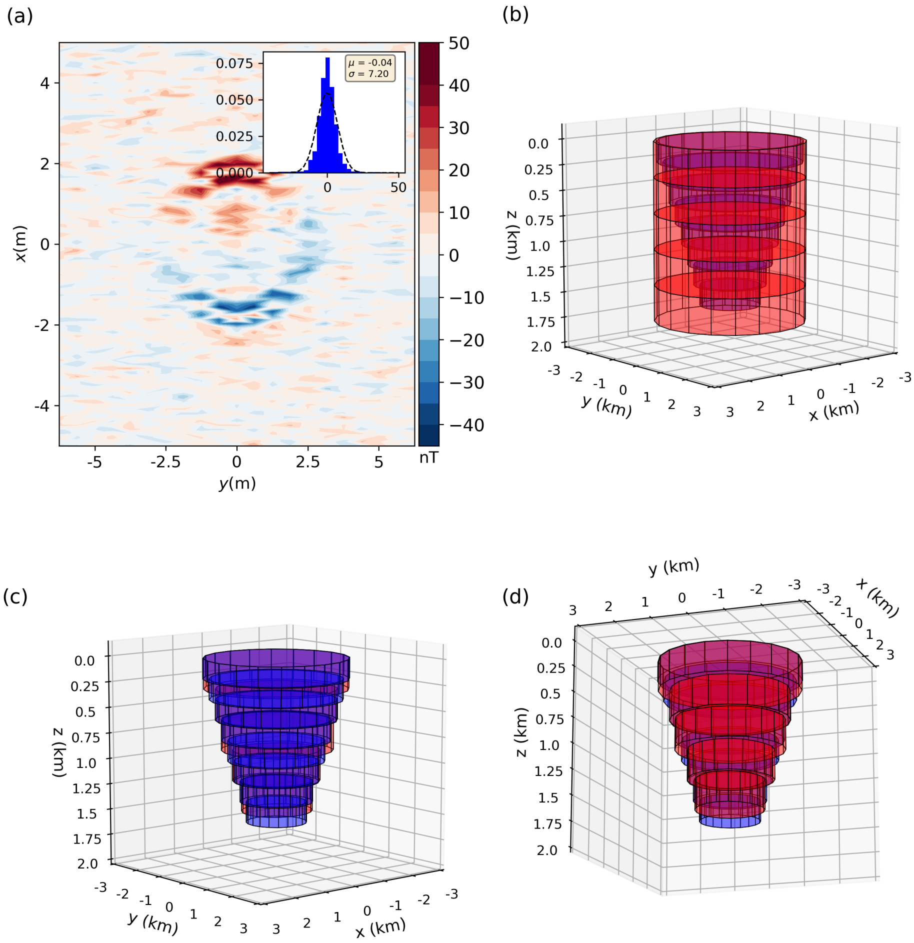

Figure 6. Application to simple model data. (a) residual data given by the difference between the noise-corrupted data (Fig. 4a) and the predicted data (not shown) produced by the estimated model. The inset in (a) shows the histogram of the residuals and the Gaussian curve (dashed line) (dashed line) whose mean and standard deviation are, respectively, $\mu = 0.04$ nT and $\sigma = 7.20$ nT. (b) perspective view of the initial approximate (red prisms) and the true model (blue prisms). (c) and (d) comparison between the estimated source (red prisms) and the true model (blue prisms) in perspective views.

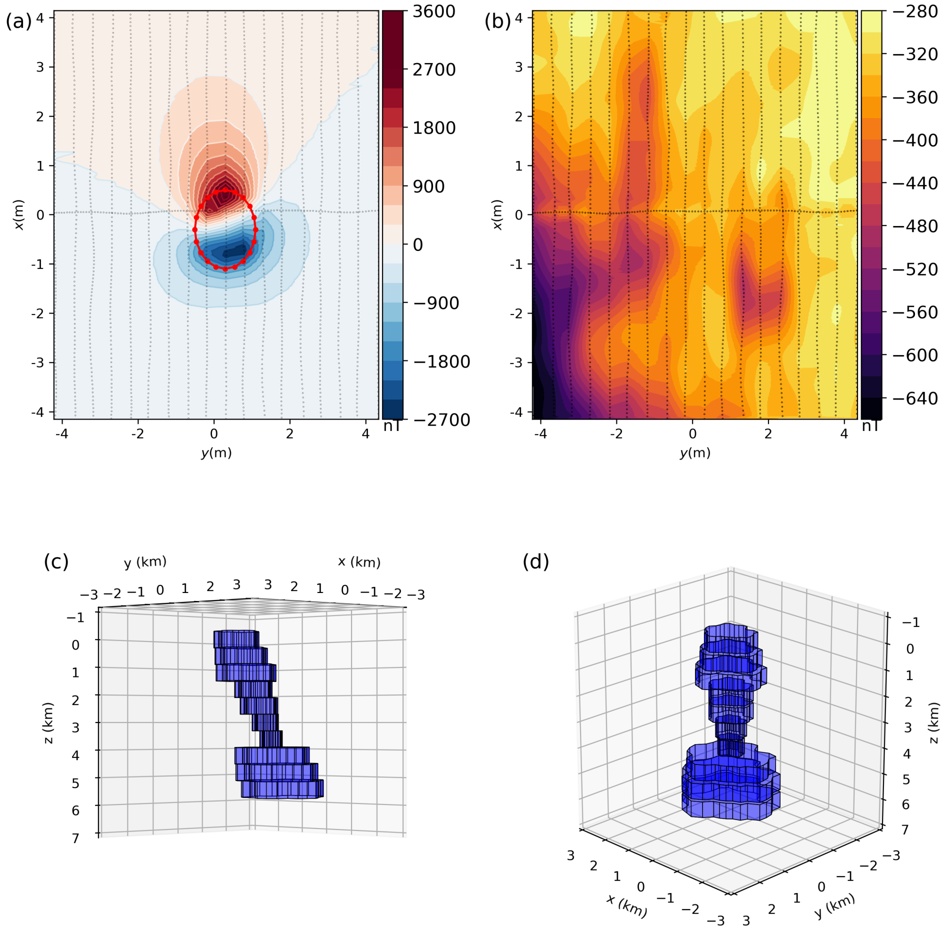

Figure 7. Complex model simulation. (a) noise-corrupted total-field anomaly with a pseudoramdom Gaussian distribution having mean $\mu_0 = 0$ nT and standar deviation $\sigma_0 = 5$ nT produced by the complex model, the black dots represent the observation points. (b) elevation of the observations simulating an airborne survey. (c) and (d) perspective views of the complex model represented by the blue prisms.

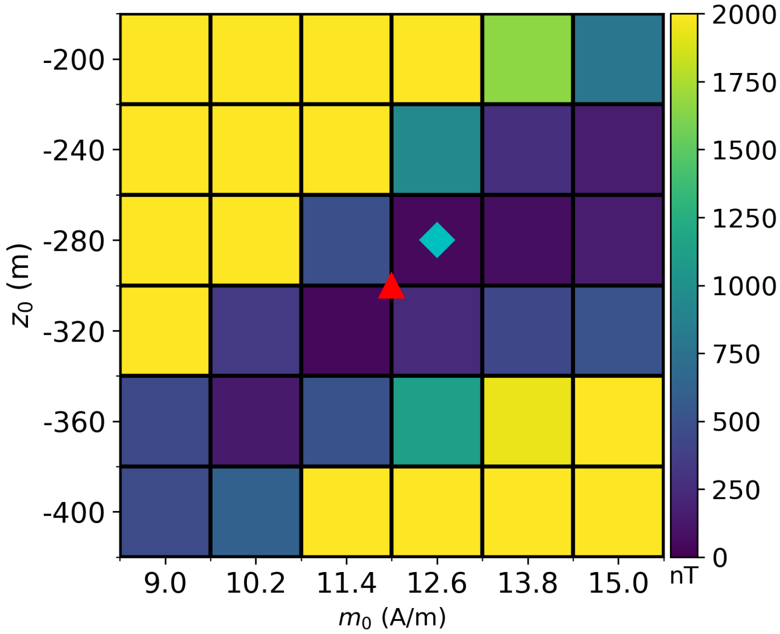

Figure 8. Validation to estimate the depth to the top (z_0) and the total-magnetization intensity (m_0) for the complex model application. The ranges in the axes are $m_0 = 9$ A/m to $m_0 = 15$ A/m with 1.2 A/m intervals and $z_0 = -400$ m to -200 m with 40 m intervals. Each square is the $\Gamma(\mathbf{p})$ (eq. 3) in nT produced by an estimated model inverted using a pair of m_0 and z_0. These 36 inversions were computed using the same cylinder as a initial approximation. The red triangle represents the true m_0 and z_0. The cyan diamond represents the estimated model that produces the lowest value for $\Gamma(\mathbf{p})$ (eq. 3).

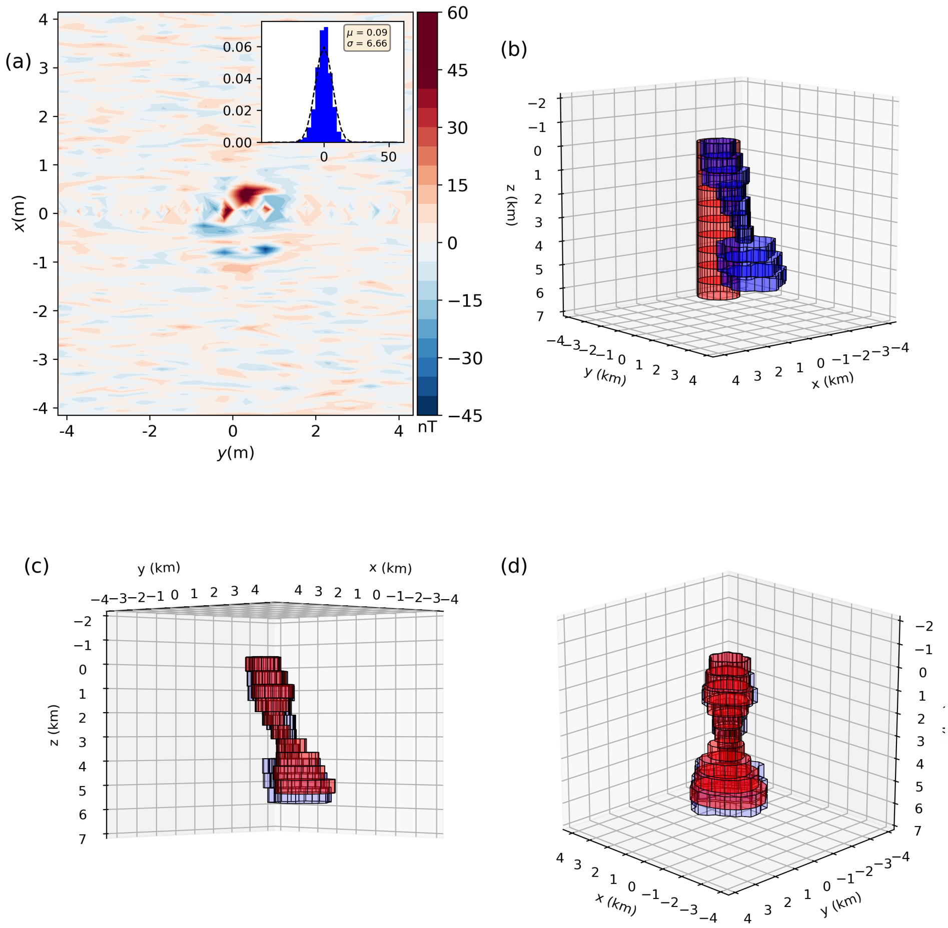

Figure 9. Application to complex model data. (a) residual data given by the difference between the noise-corrupted data (Fig. 7a) and the predicted data (not shown) produced by the estimated model. The inset in (a) shows the histogram of the residuals and the Gaussian curve (dashed line) whose mean and standard deviation are, respectively, $\mu = 0.09$ nT and $\sigma = 6.66$ nT. (b) perspective view of the initial approximate (red prisms) and the true model (blue prisms). (c) and (d) comparison between the estimated source (red prisms) and the true model (blue prisms) in perspective views.

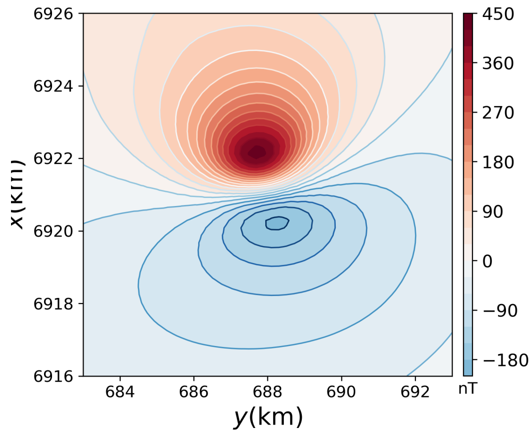

Figure 10. Total-field anomaly of the alkaline-carbonatitic complex of Anitapolis processed and calculated at $z = -2000$ m using upward continuation. The magnetic data are in nT and the coordinates are in UTM on the SAD-69 datum, with central meridian $51°$ W.

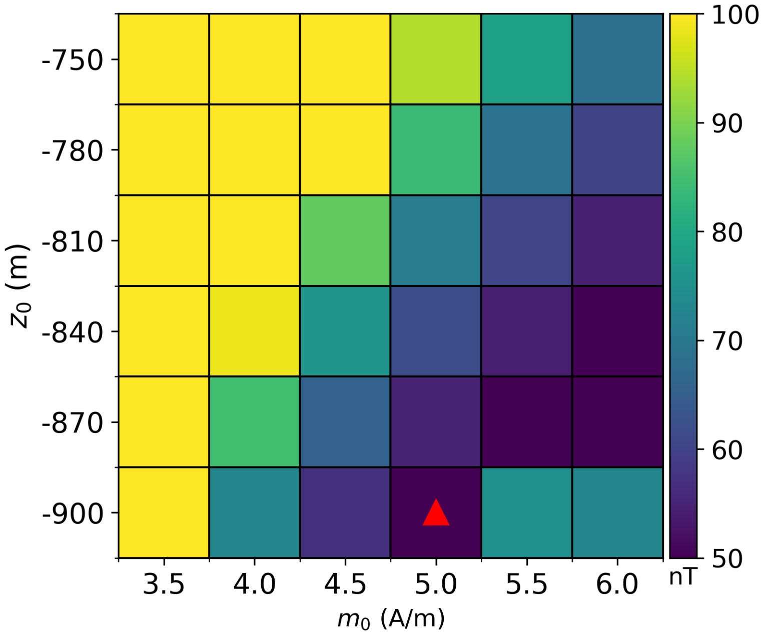

Figure 11. Validation to estimate the depth to the top (z_0) and the total-magnetization intensity (m_0) for the field application. The ranges in the axes are $m_0 = 3.5$ A/m to $m_0 = 6$ A/m with 0.5 A/m intervals and $z_0 = -900$ m to -750 m with 30 m intervals. Each square is the goal function $\Gamma(\mathbf{p})$ (eq. 3) produced by an estimated model inverted using a pair of m_0 and z_0. These 36 inversions were computed using the same cylinder as a initial approximation. The red triangle represents the lowest value of $\Gamma(\mathbf{p})$ (eq. 3).

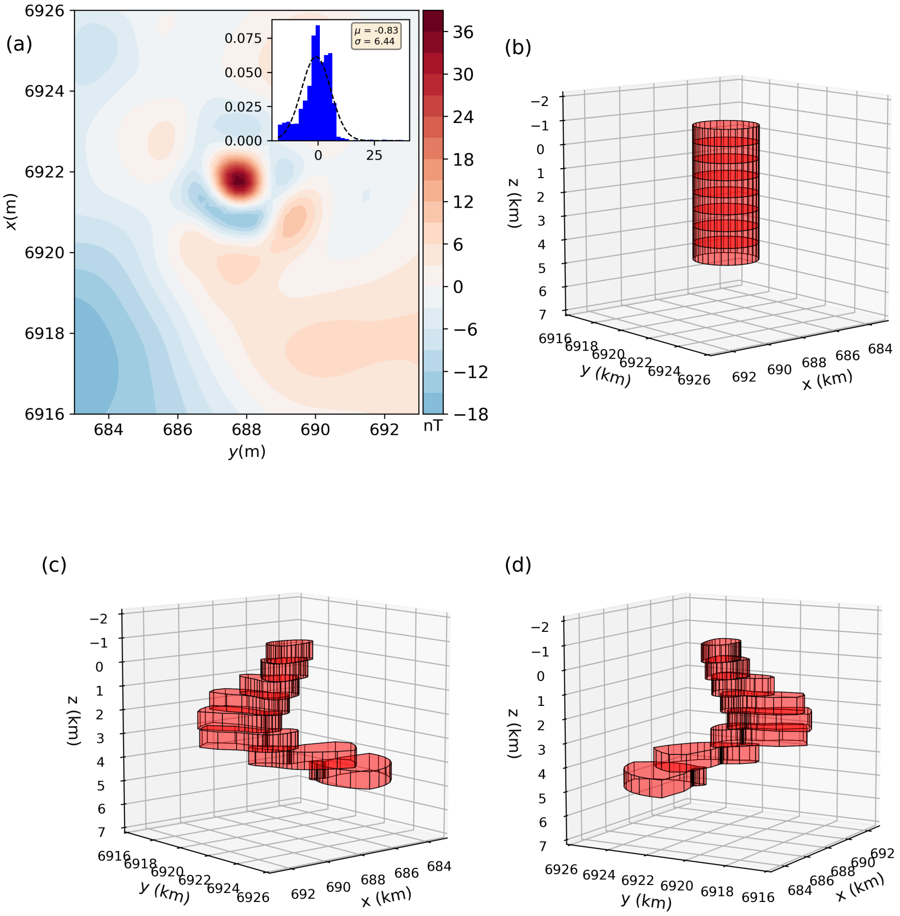

Figure 12. Application to field data. (a) residual data given by the difference between the observed data (Fig. 10a) and the predicted data (not shown). The inset in (a) shows the histogram of the residuals and the Gaussian curve (dashed line) whose mean and standard deviation are, respectively, $\mu = 0.83$ nT and $\sigma = 6.44$ nT. (b) perspective view of the initial approximate (red prisms). (c) and (d) perspective views of the estimated model (red prisms).